

Article

# Eogenetic Karst Control of Carbonate Reservoirs during a Transient Exposure: A Case Study of the Ordovician Yingshan Formation in the Northern Slope of the Tazhong Uplift, Tarim Basin, China

Yong Dan <sup>1,2,3</sup>, Liangbiao Lin <sup>2,3,\*</sup>, Bin Liang <sup>1</sup>, Qingyu Zhang <sup>1</sup>, Yu Yu <sup>2,3</sup>, Jianwen Cao <sup>1</sup> and Jingrui Li <sup>1</sup>

<sup>1</sup> Institute of Karst Geology, Chinese Academy of Geological Sciences/Karst Dynamics Laboratory, MLR & GZAR, Guilin 541004, China; danyong@karst.ac.cn (Y.D.); liangbin@karst.ac.cn (B.L.); zhangqingyu@karst.ac.cn (Q.Z.); caojianwen@karst.ac.cn (J.C.); lijingrui@karst.ac.cn (J.L.)

<sup>2</sup> State Key Laboratory of Oil and Gas Reservoir Geology and Exploitation, Chengdu University of Technology, Chengdu 610059, China; yuyucdut@163.com

<sup>3</sup> Institute of Sedimentary Geology, Chengdu University of Technology, Chengdu 610059, China

\* Correspondence: linliangbiao08@cdut.cn; Tel.: +86-135-518-99551

Received: 8 June 2018; Accepted: 7 August 2018; Published: 9 August 2018



**Abstract:** The Tazhong area of the Tarim Basin contains abundant oil and gas resources in Ordovician carbonate rocks, especially in the karst pores and caves of the Yingshan Formation. Research has indicated that the Yingshan Formation underwent a 7–11 Ma exposure during the middle Caledonian Period, resulting in large-scale karst pores and caves. However, the continental freshwater karst model cannot adequately explain the origin and distribution of karst pores and caves. In order to develop a more accurate karst model to guide petroleum exploration in the region, we analyzed the karst morphology, cave development statistics, and paleokarst environments. Karst reservoir characteristics were analyzed on the basis of the following analysis: (1) Karst morphological analyses based on core description and formation micro-imager (FMI) log analyses. The results showed that alveolar-like and Swiss cheese-like solution pores, spongy dissolution zones, pit cenotes, and small continuous karst caves developed in the Yingshan Formation. (2) The statistical analysis of pore and cave characteristics indicated that most of the karst pores and caves developed within 50 m below the unconformity where the average height of these features ranged from 0.1 to 3.0 m and their widths ranged up to 100 m. These pores and caves were commonly filled with gravel, clay, and calcite. Horizontal well and seismic attribute analysis indicated that these pores and caves were distributed over a large area. In plain view, the karst pore-cave system is comprised of cross-linked anastomosing networks of horizontal cave passages. And (3) Cathode luminescence and electron microprobe analyses suggested that clay filling within karst caves was freshwater related, while calcite filling was of seawater origin. Cements within solution pores showed three phases of luminescence, suggesting an alternating freshwater and seawater environment. Based on these characteristics, the karsts of the Yingshan Formation in the Tazhong area are interpreted to be similar to the eogenetic karsts in the Yucatan Peninsula of modern Mexico. Accordingly, this study indicates that the pore-caves of the Yingshan Formation can be subdivided into three sections. Further, the development and filling of these pore-cave sections are interpreted to have formed by eogenetic mixed-water karstification during three phases of relatively stable sea level in a coastal margin environment.

**Keywords:** eogenetic karstification; mixing zone dissolution; paleokarst reservoir; Yingshan Formation; Ordovician; Tazhong area; Tarim Basin; China

## 1. Introduction

The study of karst systems has long focused primarily on fracture-caves and geomorphology dominated by continental freshwater karsts [1,2]. As a result, studies of paleokarst-type oil and gas reservoirs used the continental freshwater karst model as a reference [3–8]. For example, the Ordovician buried-hill karst fracture-cavern that is an important oil and gas reservoir in the northern Tarim Basin [9,10] belongs to the typical continental freshwater karst model [8–12]. Previous studies suggested that the Caledonian–Hercynian tectonic movement resulted in the exposure of large-scale buried diagenetic Ordovician carbonate. This, in turn, resulted in the formation of typical Guilin-type karst peak-cluster landforms and cavern systems due to the long-term reception of meteoric freshwater karst [12,13]. This model has successfully guided the exploration of carbonate karst fracture-cavern reservoirs in the Lunnan and Tahe oil fields [14,15]. However, it is extremely rare to find diagenetic carbonate rocks that underwent long-term exposure and karstification, and continental freshwater cannot explain how karstification occurred immediately after the deposition of carbonate rocks [16]. It is theorized that the exposure time may be limited to 10 Ma (1 Ma = 1 million anniversaries) or less [17]. Vacher and Mylroie [18] identified these carbonate rocks as eogenetic karsts.

Over the past ten years, karst pores of the Yingshan Formation in the Tazhong area have generally been classified as continental freshwater karsts [19–23]. However, some special dissolution phenomena (e.g., the large-area distribution of karst caves) have recently been encountered in some drilling wells. None of the large caves are larger than 10 m. The caves are generally small, with a large width/height ratio [23,24] and are filled with clay [20]. In addition, the failure of oil and gas exploration to utilize the continental freshwater karst model suggests that the model may not be adequate to predict the distribution of fracture-cavern reservoirs in the Yingshan Formation in the northern slope of the Tazhong area. Yu et al. [24] proposed that the formation of these karst caves could be attributed to fault karst dissolution, but the genesis of karst caves away from faults was not well explained. In fact, the geological history of this region suggests that the exposure of the Yingshan Formation carbonate in the Tazhong area may be limited, ranging from a few to several dozen Ma [25]. Dan et al. [17] speculated that the Yingshan Formation carbonate karst in the northern slope of the Tazhong area may be an eogenetic karst. Several studies conducted a preliminary analysis of the Yingshan Formation paleokarst in the northern slope of the Tazhong area [26,27]. However, these studies did not provide geochemical evidence or recognize the eogenetic karst pattern in this area.

The study of paleokarst pore-caves under transient exposure conditions during the geological history of the Yingshan Formation is important for enriching paleokarst theories and serving as a guide to oil and gas exploration. The goal of this study was to provide evidence that the paleokarst of the Yingshan Formation in the northern slope of the Tazhong area is an eogenetic karst by utilizing data from the oilfield. This study identified paleokarst phenomena, carried out development statistics on the solution pore-cave system, and analyzed fillings in pores-caves in order to identify the characteristics and environment of the Yingshan Formation paleokarst. The interpretation of the paleokarst pattern was then based on discussion of the morphological features of the paleokarst, development features of the pore-cave system, analysis of the paleokarst environment, and comparison with modern karstification. Thus, the study of paleokarst pore-cave genesis is important for theoretical and practical applications.

## 2. Geologic Setting

The Tazhong Uplift lies in the central part of the Tarim Basin in northwestern China. The uplift extends to the northwest and is bordered by the Bachu Fault Uplift to the west, the Tadong Low Uplift to the east, the Manjiaer Depression to the north, and the Tangguzibasi Depression to the south [28,29]. From north to south, the Tazhong Uplift can be divided into three third-order structural belts [22], namely the Northern Slope belt, the Central Fault horst belt, and the Southern Slope belt. The study area was located in the Northern Slope belt (Figure 1a,c). There are two important targets when exploring the carbonate formations in the Tazhong area: (1) the reef-bank reservoir in the Lianglitage

Formation [30], and (2) the paleokarst weathering crust reservoir in the Yingshan Formation [22]. Pores, caves, and fractures formed by exposed karst have been identified as the main Yingshan Formation reservoir types in the northern slope of the Tazhong area since the commencement of exploration in 2006 [19].

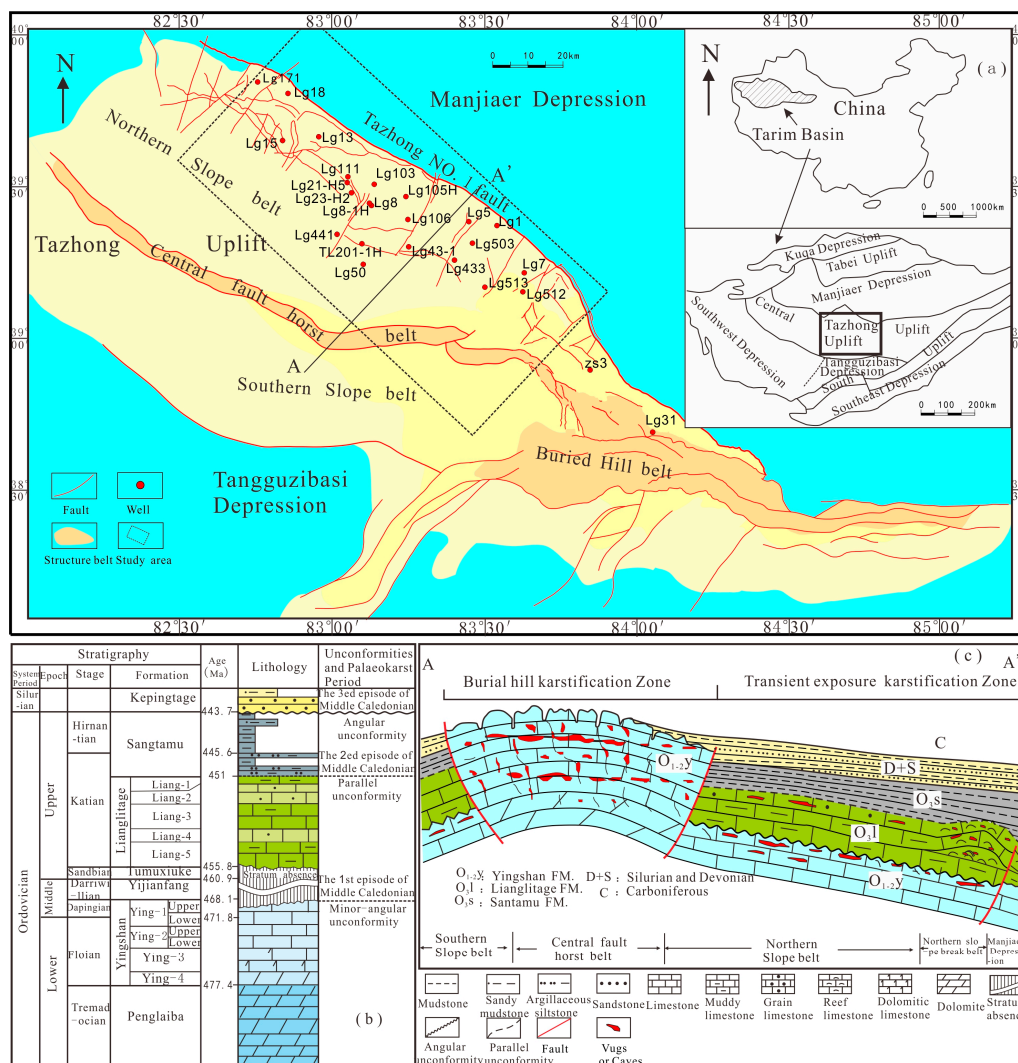


**Figure 1.** The location and geological setting of the study area. (a) Tectonic division of the Tazhong Uplift and the location of the study area [22]; (b) Generalized stratigraphy and associated unconformities (Northern Slope belt) of the Ordovician in the study area. The stages and ages are from the International Commission on Stratigraphy (2014); (c) Karstification division of the Tazhong Uplift and the location of the Northern Slope belt.

Previous studies have indicated that carbonate platform-facies comprising of calcarenite and micrite were deposited in the Yingshan Formation during the early Ordovician [31]. During the later stage of the early Ordovician, the area was affected by the first episode of the middle Caledonian, resulting in the uplift of carbonate rock in the Yijianfang and Yingshan formations immediately after deposition, leading to carbonate platform exposure and intense karstification [25,27] (Figure 1b). The erosion of the upper parts of the uplifted formations resulted in large sections of missing strata, primarily in the middle Ordovician Yijianfang and Tumuxiuke formations at the base of the Upper Ordovician. The lower Ordovician Yingshan Formation was also eroded, with the degree of erosion increasing from north to south. The time break between the Yingshan Formation and the Lianglitage

Formation was on the order of 12–15 Ma [25,27]. The exposure time of the Yingshan Formation after the deposition of the Yijianfang Formation (Figure 1b,c) was only 7–11 Ma, resulting in the formation of the present-day unconformity. The Yingshan Formation can be divided into four members (Figure 1b). The Ying-1 and Ying-2 members are composed of approximately 300 m of pure limestone, and the Ying-3 and Ying-4 members comprise dolomite-bearing limestone and dolomite. Limestone of the Ying-1 and Ying-2 members is exposed at the top of the Yingshan Formation. The exposure and subsequent weathering of these carbonates led to the formation of large amounts of fractures and caves that constitute a significant portion of the oil and gas carbonate reservoirs in the Tarim Basin [20].

### 3. Methods

About 90 wells were drilled in the Yingshan Formation on the Northern Slope of the Tazhong Area, where 15 wells were cored and 25 wells underwent image logging. All wells underwent conventional logging. In addition, three-dimensional seismic data acquisition was carried out across the whole study area. All of these provided a solid database for the present study. Abundant formation micro-imager (FMI) logs and cores provided reliable data for distinguishing paleokarst-related phenomena in detail. Core-calibrated FMI logs were used to identify fractures and paleokarst features. Conventional logs, in particular, gamma-ray (GR) and resistivity (Rt) logs, were also used as auxiliary sources for the identification of karst features, such as clay-filled caves that were indicated by an extremely high gamma-ray count. Seismic data, with a bin size of 25 m × 25 m characterized by an effective frequency ranging from 10–30 Hz, covered some 3500 km<sup>2</sup>. The impedance contrast between the Yingshan Formation and the overlying Lianglitage Formation was small, and reflections corresponding to the top of the Yingshan Formation were weak. Conversely, the large acoustic impedance contrast between the paleocave system and host rocks gave rise to strong reflections highlighted as “bright spots” against the weak reflections of interfaces. In order to better understand the formation environment of paleokarst and determine the type of paleokarst, 15 samples were taken continuously from the cave and its surrounding rock in Well ZG43-1. On the basis of thin-section identification, samples were selected for cathode luminescence analysis and electron microprobe analysis to determine the nature of pore and cave cements and fillings. The testing and analysis methods are described in the following.

#### 3.1. Rock Thin-Section Preparation and Identification

The rock sample was bonded to a glass slide with a non-luminous epoxy resin and ground to a thickness of 0.03–0.06 mm. To meet the requirements of cathode luminescence and electron probe analysis, the surface of the standard thin-section was then highly polished. The thin sections were analyzed under optical plane-polarized light at magnifications ranging from 50× to 500×. A petrographic examination was performed using a Leica Imager microscope-photometer.

#### 3.2. Cathode Luminescence Analysis

Following identification from the thin section, the cathode luminescence analysis focused on the calcite filling from five pores in the surrounding rock and eight fillings in the caverns. The same test conditions, using a beam voltage of 17 kV and a beam current of 500 μA, were performed on all samples. The instrument used for cathode luminescence analysis was a CL8200 MK5 cathode luminescence analyzer produced by CITL in the United Kingdom (in conjunction with a Leica polarizing microscope).

#### 3.3. Electron Microprobe Analysis

An electron beam bombarded the surface of a number of delineated measuring points to generate X-rays. The wavelengths of emitted X-rays were then analyzed using the spectrum analysis method to determine the elemental composition of each measuring point. The experimental conditions were as follows: temperature 25 °C, acceleration voltage 15 kV, beam intensity 10 nA, beam spot diameter 10 μm, detection angle of 52.5°, and correction method ZAF3. Electron microprobe analysis was conducted using an EPMA-1720 H Series analyzer produced by the Shimadzu Corporation. The same

test conditions were performed on all samples. The detection limits of EPMA differ for each element and are affected by the overall composition of a sample and the analytical conditions. For most elements, the detection limits for EPMA is between 30 and 300 parts per million (ppm), and with relative errors of 2%.

The analyses, as outlined above, were conducted at the State Key Laboratory of Oil and Gas Reservoir Geology and Exploitation, Chengdu University of Technology, Chengdu, China.

#### 4. Paleokarst Characteristics

The Tazhong area is located beneath the Taklimakan Desert. No rocks of the Yingshan Formation rocks are exposed. Therefore, the study of paleokarst dissolution characteristics was based primarily on the core from 15 wells and image logs from 25 wells.

##### 4.1. Dissolution Characteristics in the Core

Observations in the core from 15 wells indicate that c. 1 mm solution pores and c. 0.6 m caves are developed near the unconformity. Some solution pores are developed in selected structure–texture positions, are evenly distributed, and occur as alveolus shapes (Figure 2a,b) with pore sizes of <5 mm and densities of 1–3 pores per cm. Some relatively large pores and caves are developed along bedding planes (Figure 2d,e) and occur as tabular configurations. Here, the pores and caves have unclear interfaces with the wall rocks. They commonly display gradual transition features and “easily blooming” characteristics (Figure 2e). Calcareous crust growths and lacery dissolution are observed along the pore-cave margins (Figure 2d,e). Tabular solution pores are filled with carbonate cement. The tabular shape or deformation may indicate compaction after pore formation. Figure 2g shows Swiss cheese-like pores that are filled with clay. These pores fully show the dissolution-filling characteristics of the eogenetic stage when carbonate rocks were not consolidated. Some dissolution phenomena without texture–structure selectivity was also observed. For example, Figure 3c,f show dissolution fractures filled with argillaceous matter, and Figure 2h shows the inside of solution caves where both dissolution dissociation breccias and clay are observed. These characteristics reflect the paleokarstification of the Yingshan Formation.



Figure 2. Cont.



**Figure 2.** The dissolution of pores and caves developed in the carbonate rocks of the Yingshan Formation during weak diagenesis in the Tazhong area. (a) Honeycomb-like solution pores in calcarenite, Well TL452, 6463.2 m; (b) Alveolus pores and caves in argillaceous micrite with sizes of <1 cm, wholly filled with calcite, Well LG 106-1h, 6028 m; (c) Dilatant fractures filled with argillaceous matter, Well LG111, 6109.5 m; (d,e) Tabular pores developed along the bedding; pores do not show clear contacts with wall rocks, commonly showing gradual transition and “easily blooming” characteristics. Calcareous crusts and lacery configuration are commonly observable, fully or half-filled with calcite, particularly bitumen, with 2 cm-sized pores, Well LG7, 5835–5838 m; (f) Solution fractures filled with argillaceous matter, Well LG105H, 6201.4 m; (g) Swiss cheese-like solution pores, evenly distributed and filled with argillaceous matter, Well LG512, 5483.7 m; (h) Solution karst caves, filled with clay and breccia, Well TL201-1h, 5460.9 m; (i) Karst caves, 0.6 m high and fully filled with clay and breccia, Well LG43-1, 5288.5–5289.1 m.

#### 4.2. Dissolution Characteristics in FMI Logs

The dissolution characteristics of pores and caves can be directly observed in the core. However, due to the high cost of coring and the difficulty in drilling deep wells in the oil field, only shorter cores were cut. Hence, the observed solution phenomena are the “tip of the iceberg” relative to the solution characteristics of the whole area. Additionally, the cores cannot be cut through some large pore-cave intervals. Consequently, only a limited understanding of the solution characteristics of karst pores can be obtained from the core. Therefore, drill-hole image logs are necessary to supplement the deficiency of core observations. The establishment of pore-cave identification relationships using core-image logs can help identify both larger pores and caves and more dissolution characteristics over uncored intervals.

Previous scholars have studied the core and image logging relationships of solution pores and caves in the Tazhong area and provided interpretations of typical images from FMI logs [24].

(1) Solution pores (Figure 3a): These show low-resistivity and medium GR characteristics and appear as densely developed dark spots on FMI logs. Pores are generally developed along bedding. Figure 3a shows pores in the core that are not filled (some pores are filled with mud or calcite). (2) Cave fillings (Figure 3b): Principally comprise clay and calcite. Clay has low resistivity, a high GR, and occurs as a dark blocky configuration on FMI logs. In contrast, calcite fillings have extremely high resistivity and occur as light spots and a blocky configuration on logs. (3) Karst cave breccias (Figure 3c): Formed by crushed bedrock, display color consistent with bedrock, and are surrounded by dark karst cave mudstone on FMI logs.

By using FMI log data to identify and interpret the four classes of high-GR combination forms in the Yingshan Formation, three distinct zones of dissolution combination phenomena were also found:

(1) Spongy-like dissolution zone (containing single-bed or multi-bed karst caves): The first zone shows a unimodal or unidentate high-GR (Figure 4) or multimodal high-GR interval (Figure 5). Image logs show that each high GR peak corresponds to a karst cave, and the height of a single karst cave varies from 0.5–1.5 m (Figure 4). The multi-modal curve indicates 2–3 karst caves (Figure 5), and Swiss cheese-like pores and spongy-like dissolution have developed at the top and bottom of karst caves. Therefore, a dissolution zone comprising of single- or multi-bed karst caves and spongy Swiss cheese-like dissolution has developed over a height of 1–15 m (Figure 4).

(2) Pit cenote: These zones are box-shaped and display high-GR intervals on downhole logs. The pit cenotes are depicted on image logs as a large set of mudstone-filled intervals (Figure 6). Since the pit cenotes are in direct contact with the limestone of the Lianglitage Formation, it is concluded

here that mudstone from the Lianglitage Formation filled the pit cenotes and formed a large set of high-GR intervals, some with a thickness of 20 m.

(3) Horizontally continuous karst caves: Multiple horizontal wells in the study area intersect continuously and with intermittently high-GR curves in the Yingshan Formation (Figure 7). According to image logs, each peak is a high-GR-filled karst cave (Figure 7). In Well LG23-h2, 41 caves larger than 10 cm were identified with a maximum width of up to 110 m (Figure 10). The horizontal extent of small caves is abruptly contained due to interlayering of bedrock and limestone that forms the partition between individual cave bodies (Figure 10). This phenomenon was also observed in the horizontal well LG21-H5 for approximately 100 m, where three caves with widths ranging from 4–40 m intersected. Adjacent caves show low GR and high resistivity together with well-developed pores and fractures (Figure 7).

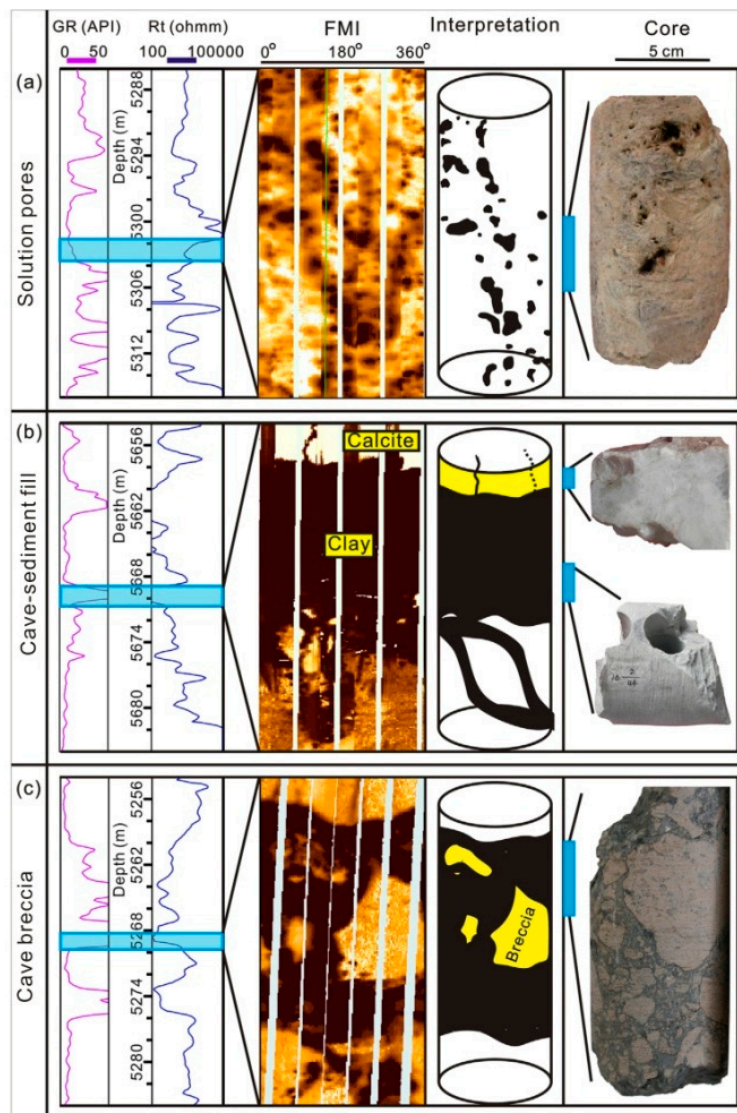


**Figure 3.** The identification of paleokarst features from the formation micro-imager (FMI) logs and auxiliary conventional logs. Each paleokarst feature is interpreted from FMI logs and core samples [26]. (a) The core and image logging relationships of solution pores; (b) The core and image logging relationships of cave fillings; (c) The core and image logging relationships of cave breccias. GR: gamma ray; Rt: true formation resistivity.

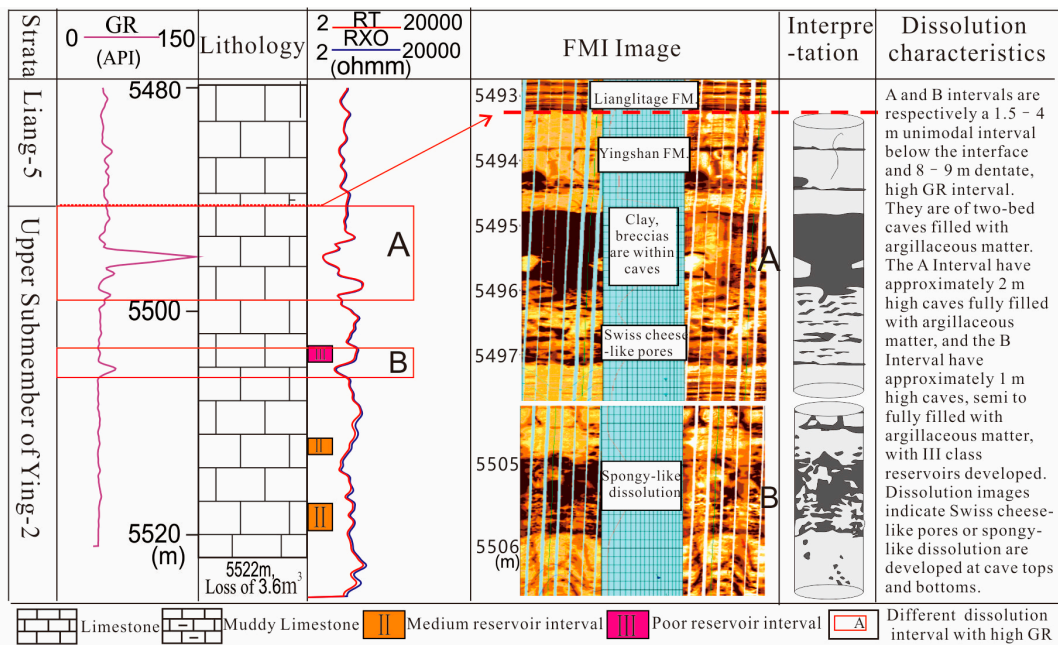


**Figure 4.** The unimodal (or unidentate) high-GR intervals indicate a spongy dissolution zone, which is composed of one karst cave and Swiss cheese-like solution pores in Well LG441. RXO: flushed zone formation resistivity.

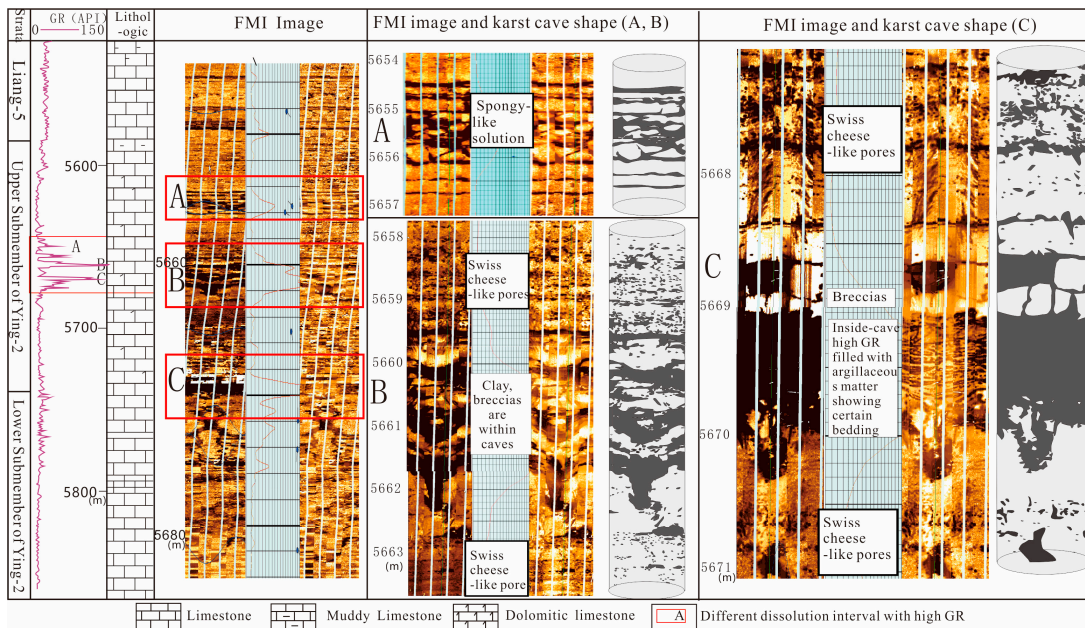


**Figure 5.** The multi-modal high GR interval indicates a spongy dissolution zone, composed of many small karst caves and Swiss cheese-like solution pores in Well LG433. A, B, and C represent different peaks of the multi-modal high-GR interval in Well LG433. According to image logging, A indicates a spongy dissolution, which is approximately 1.5 m high. B indicates three small-sized karst caves (each cave is approximately 0.5 m high) and the Swiss cheese-like solution pores. A, B, and C vertically constitute a spongy dissolution zone, approximately 15 m in height, which comprises multiple small-sized karst caves and Swiss cheese-like solution pores.

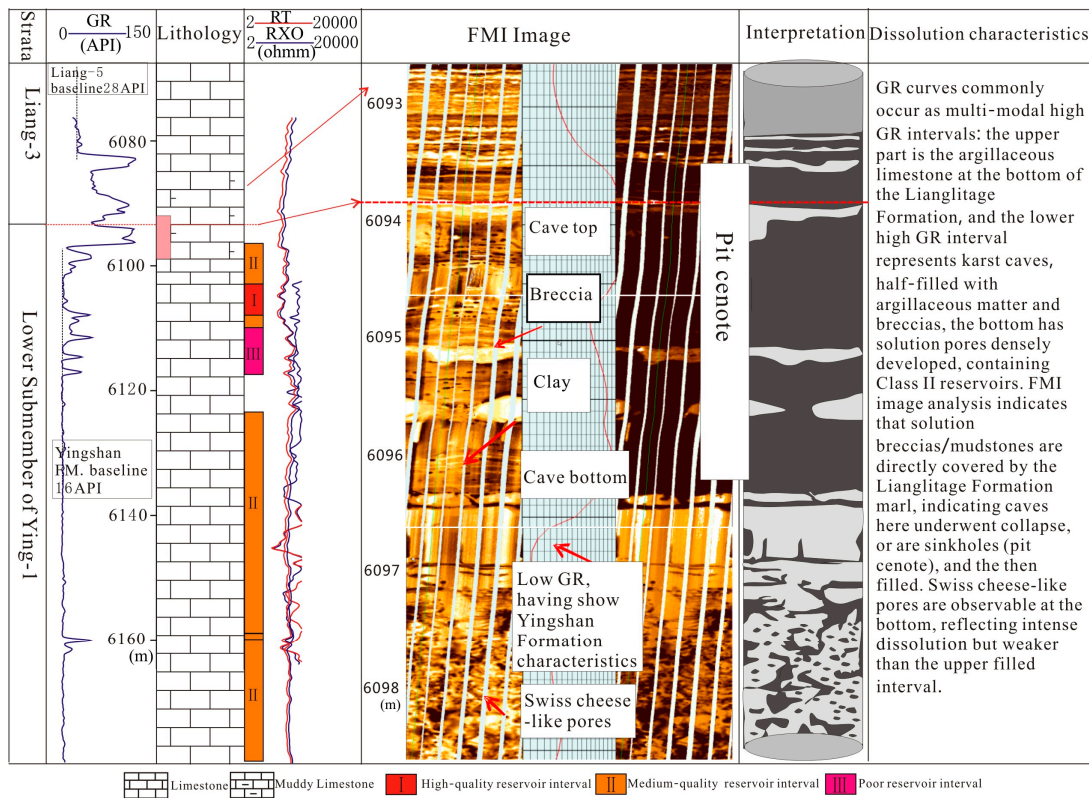


Figure 6. The high-GR interval represents an interpreted pit cenote in Well LG111.

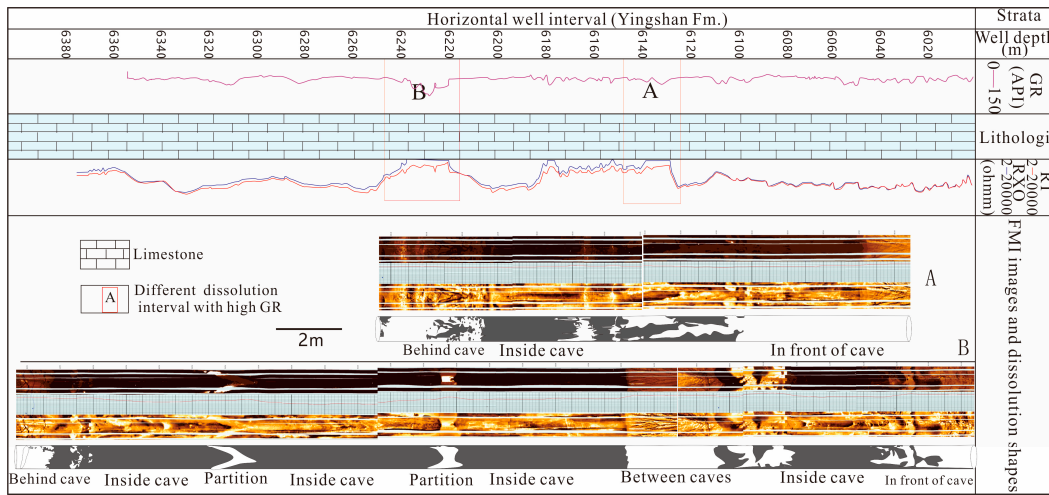


Figure 7. The continuous high-GR intervals indicate small karst caves in horizontal wells (LG21-H5).

## 5. Development Characteristics of Paleokarst Cave Systems

### 5.1. Statistics of Pore-Cave Development

After 2006, an increasing number of wells were drilled in the Yingshan Formation in the northern slope of the Tazhong area. Approximately 90 wells have been drilled to date.

Based on tests from about 200 cores in the Yingshan Formation, the carbonate rocks had an average porosity of 0.91% and an average permeability of  $3.76 \times 10^{-3} \mu\text{m}^2$  [19], indicating a relatively low-porosity and low-permeability bedrock. The reservoir mostly contained secondary solution pores and caves formed by karstification with strong heterogeneity.

Drilling and mud logging data together with the interpretation of downhole logs and images from FMI logs provided the data for pore-cave statistical analysis. The results are as follows.

- (1) Drilling and mud logging data indicate some 25 intervals of blow-off/loss/overflow in more than 90 Yingshan Formation wells. About 92% of these intervals had vertical blow-off lengths of <3 m, and only two intervals had vertical blow-off lengths of about 4 m (the first and second intervals had a vertical blow-off length of 4.2 m and 4.3 m, respectively).
- (2) Interpretation of some 72 wells with conventional logging data (e.g., GR and Rt curves) indicated a total of 213 poor-quality reservoir intervals. The majority of reservoirs (about 54%) in the Yingshan Formation were found at least 50 m below the unconformity, and about 31% of the reservoir intervals were found 50–150 m below the unconformity. About 51% of the reservoir intervals had a thickness of <5 m (Figure 8a). Seventy-eight high-quality reservoir intervals were identified out of a total of 213 reservoir intervals, including 16 unfilled cave reservoirs and 60 unfilled fracture-cave reservoir intervals. Based on log analysis, 56 high-GR-filled intervals with heights ranging from 1–15 m were found. Each high-GR filling interval was a dissolution zone containing at least one smaller filled karst caves in the vertical direction, where the average height of a single small karst cave was <3 m. Pore-caves in the study area were mostly filled and displayed high GR on logs. Additionally, statistical analysis shows that reservoir intervals were generally found in the lower parts of filled intervals (Figure 8b).

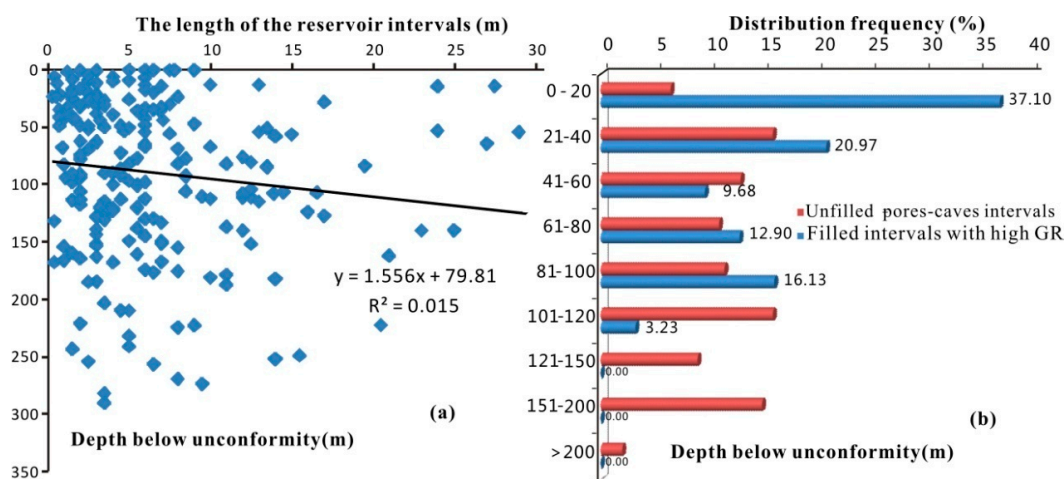


**Figure 8.** The distribution and fill characteristics of reservoir intervals below the Yingshan Formation unconformity. (a) Development scale of fracture-cave intervals in drilled wells in the Tazhong area and depth of the Yingshan Formation unconformity; (b) Distribution characteristics of argillaceous-filled caves and unfilled caves.

- (3) FMI data from 19 wells indicated that there were five wells with >40 cm-sized caves. There were 14 wells that intersected 34 caves; 91% of the caves were <3 m high, and 50% of the caves were <1 m high (Figure 9a). The caves were found over discrete intervals below the top of the Yingshan Formation: 17 caves within 30–50 m, 6 caves within 0–10 m, and 3 caves within 50 m below the formation top.
- (4) FMI data from six horizontal wells indicated that two wells did not intersect >40 cm-sized caves, and four wells intersected 65 caves (including intermittently distributed caves in one horizontal well). Most of the caves had widths between 1–2 m, and several caves had widths or lengths greater than 10 m, and even up to 100 m (Figure 9b).

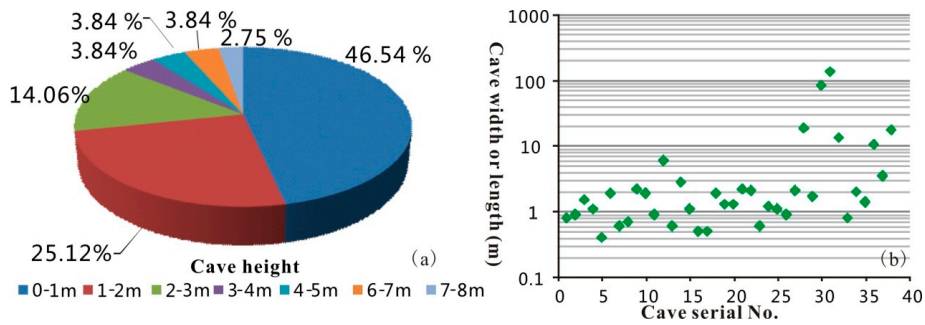


**Figure 9.** The statistics of caves intersected by drilling wells according to FMI log data. (a) Height statistics of caves intersected by vertical wells according to FMI log data; (b) Average width of caves intersected by horizontal wells based on the FMI logs.

5.2. Distribution Characteristics of Paleokarst Pores and Caves

The analysis of dissolution characteristics (Section 3.2) indicates that pores and caves were developed within 1–15 m high dissolution zones. The height of a single karst cave generally ranged between 0.1–3 m, and statistical analysis shows that only 1–3 vertical dissolution zones could be developed at most. In addition, horizontal wells showed that multiple horizontal high-GR intervals could be continuously developed. These were composed of multiple-filled karst caves where the width of a single karst cave could range from several meters to hundreds of meters (Figure 10). Comparison of these horizontal wells with seismic sections was conducted to establish well-seismic correlations. Flaky weak reflections were observed on seismic sections (Figure 10a). Coherent spectral analysis techniques found that flaky reflection was widely developed in seismic sections from the northern slope of the Tazhong area, with an area of up to 331 km<sup>2</sup> (Figure 11). Analysis of 90 wells in the Yingshan Formation found that more than 50 wells encountered high-GR karst cave-filled intervals.

A comprehensive analysis of single karst caves found that they displayed relatively small heights but a large range in widths. Karst caves had relatively large width/height ratios and mostly showed a layered, large-area distribution. These karst cave systems were interpreted as cross-linked anastomosing networks composed of horizontal cave passages in space, where the majority of pore space were filled with argillaceous matter. Minor filled reservoirs occurred in the lower part of filled intervals.

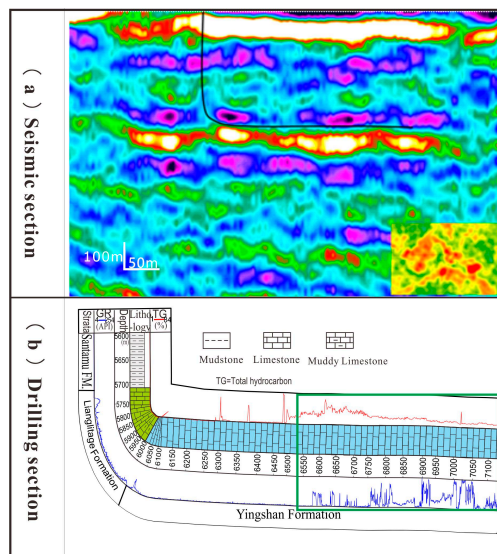


**Figure 10.** Cont.

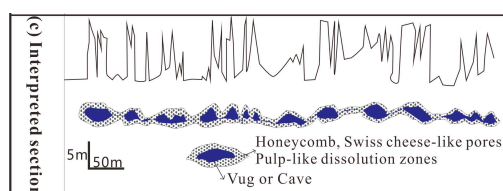


**Figure 10.** The corresponding characteristics between high-GR intervals and seismic reflection. (a) Flaky reflections in the northern slope of the Tazhong area comprise multiple weak “strings of beads” (or weak bright spots); (b) the horizontal drilling in Well LG23-H2 displays multi-intervals with high GR, and a total length of above 500 m; (c) Continuous small karst pores and caves from FMI log interpretation.

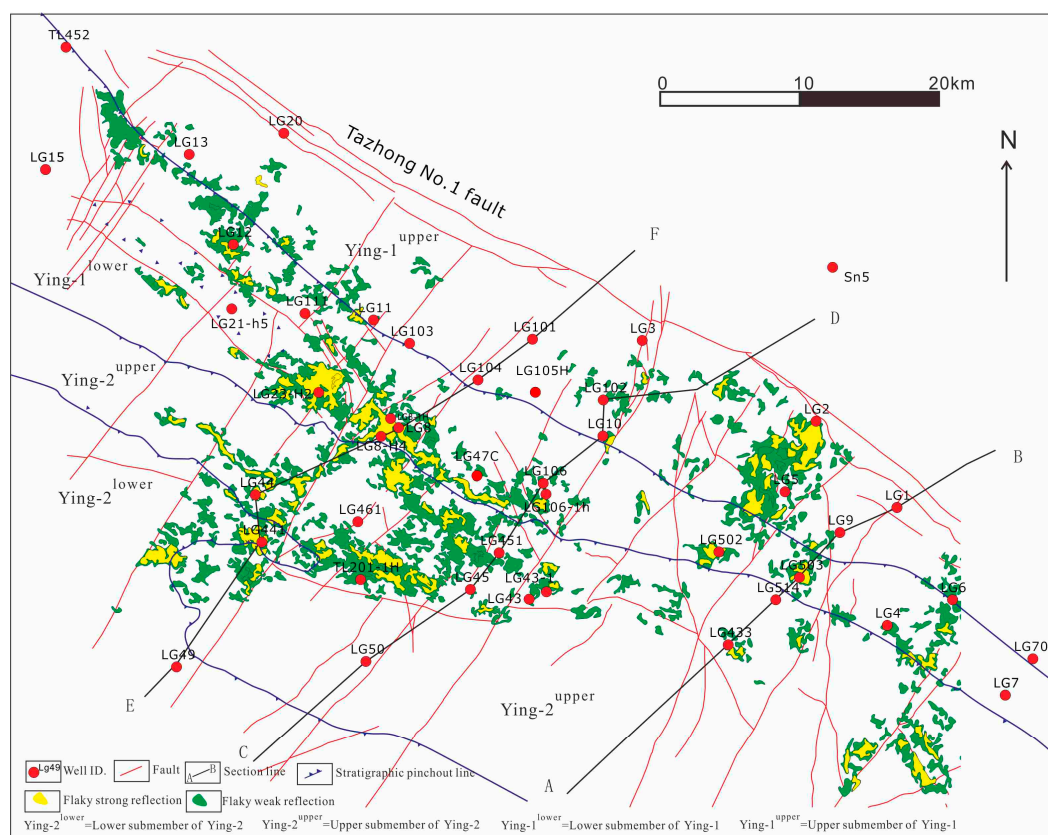


**Figure 11.** The distribution of flaky reflection from analysis of root mean square amplitude (RMSA) attribute 0–60 ms (0–180 m) below the top of the Yingshan Formation.

### 6. Geochemical Characteristics of Paleokarst Cave Fillings

Samples were systematically collected from karst cave intervals. Samples from the upper and lower parts of the karst cave interval in Well LG43-1 were cut for 15 thin sections then polished, and the fillings were analyzed using cathode luminescence and electron microprobe techniques to determine the filling characteristics.

Core observations indicated that pore karst caves in Well LG43-1 were 60 cm high (Figure 3i), and thin-section analysis indicated that the bedrock at the top and bottom of karst caves was mainly composed of calcarenite (Figure 12a,c,e,k). The karst caves were filled with clay, limestone debris, calcite, and limestone gravel (Figure 12g,i). In total, the fillings were composed of 45% clay, 40% limestone debris, and 5% calcite or calcareous cement.

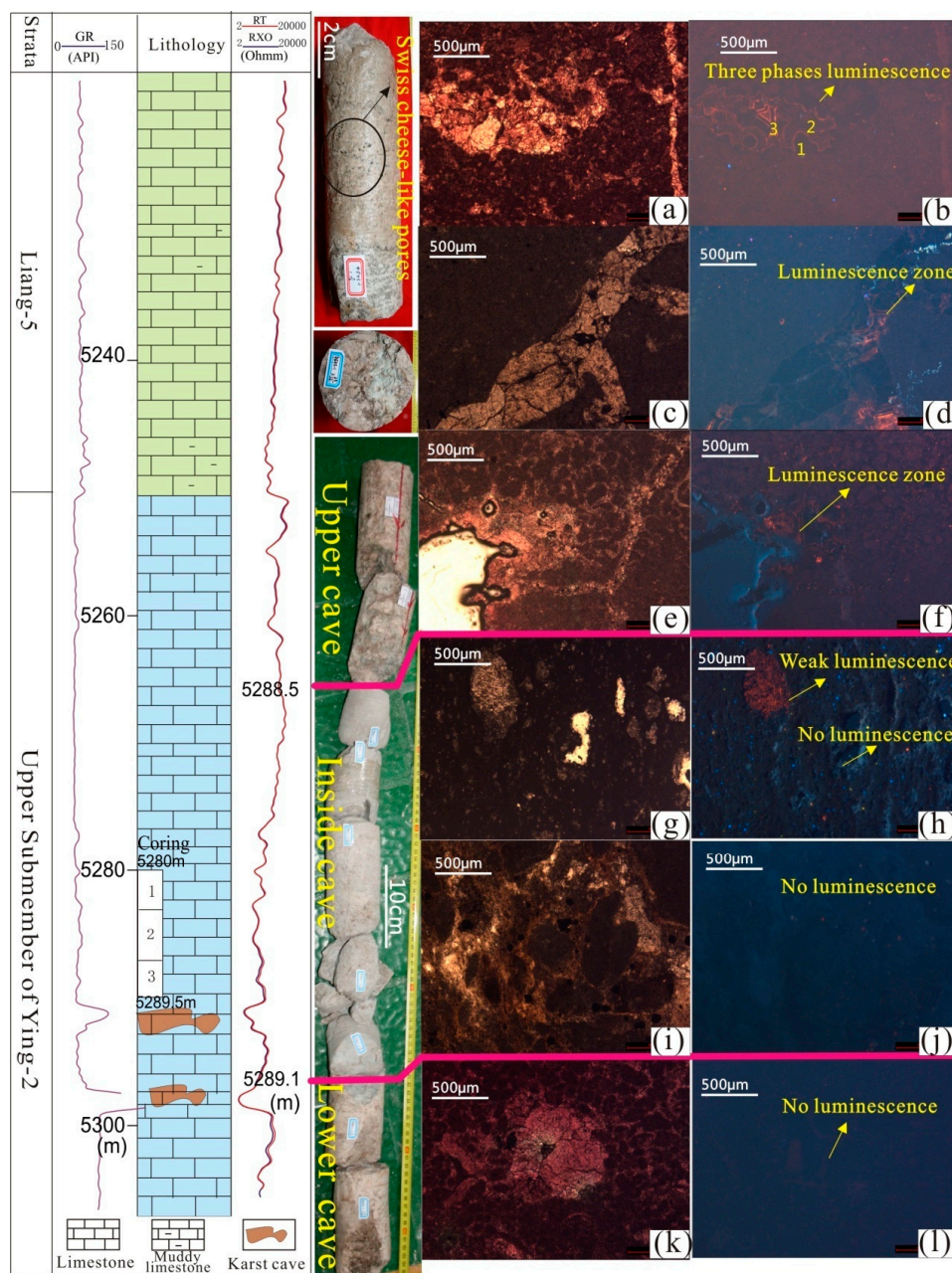


**Figure 12.** The cathode luminescence characteristics of karst pore and cave fillings of the Yingshan Formation in Well LG43-1. (a,b) Three phases of luminescence inside karst pores, 5282.8 m; (c,d) Calcite inside karst fractures showing weak luminescence zoning, 5283.7 m; (e,f) Weak luminescence zoning in pores in calcarenite, 5288.4 m; (g,i) Limestone debris grains, clay, calcite, and dolomite inside karst caves. Generally, fillings in karst caves did not show luminescence (j) and minor calcite showed weak luminescence (h); 5288.5–5289.1 m; (k,l) Calcite in pores at the lower part of karst caves did not show luminescence, 5289.2 m.

### 6.1. Cathode Luminescence Characteristics of Pore Fillings and Identification of Paleokarst Environment

The use of cathode luminescence is particularly advantageous for the identification of paleokarst environments because these environments have strong cathode luminescence features. Huang [32] postulated that strong cathode luminescence features are affected by two aspects: (1) The cathode luminescence of carbonates is mainly controlled by Mn and Fe content. Mn acts as an activator, causing cathode luminescence features to appear in carbonates, while Fe acts as a quencher, thereby

inhibiting luminescence. Previous studies have indicated that differences in Fe and Mn content can affect luminescence. Fe only begins to affect luminescence to a greater degree than Mn once the Fe content is greater than 5000 ppm. Additionally, cathode luminescence of carbonate rocks can only be totally quenched when the Fe content is greater than 10,000 ppm. Examples of the latter case are extremely rare because there are very few samples with Fe content greater than 10,000 ppm on the unconformity. This suggests that the cathode luminescence of most carbonate minerals is more closely related to the Mn content than Fe content. (2)  $Mn^{2+}$  has a larger solubility than  $Fe^{2+}$  within a broad range of Eh values. As a result,  $Mn^{2+}$  can appear in more oxidized water, making calcite cement in karst environments richer in  $Mn^{2+}$  and poor in  $Fe^{2+}$  content, resulting in a higher luminescence.

When studying the Ordovician paleokarst breccias of the northern Tarim area, Huang [33] discovered that gravels commonly indicated seawater with low Mn content and with weak or no luminescence. Inter-gravel cements of meteoric water origin contained high Mn concentrations and displayed strong luminescence (Fe content in a meteoric water environment, as a chemical precipitate, is limited). Further, cements with luminescence zoning develop in karst environments, particularly within carbonate rock cements formed in atmospheric undercurrent environments. Mussman and Read [34] discussed this zoning variation. The following are cathode luminescence features of Well LG43-1.

**Upper Karst cave:** Solution pores were densely developed with diameters of approximately 1 mm, some of which were filled with calcite (Figure 12). The cathode luminescence analysis of calcareous cements in solution pores (Figure 12a) identified three phases of luminescence zones: Phase 1 occurred along margins inside pores as indented calcite showing weak, dark luminescence but light zoning; Phase 2 showed weak, orange-red luminescence; and Phase 3 occurred in the central parts of pores and displayed alternating light–dark luminescence zoning (Figure 12a,b). Additionally, luminescence zoning could be observed in some solution fractures and pores, but only showing one phase (Figure 12d,f). Different luminescence zones represent different fluid properties.

**Inside karst cave:** Generally, karst cave fillings did not show luminescence (Figure 12i,j), and minor calcite content showed weak luminescence (Figure 12h).

**Lower karst cave:** Calcite in bedrock pores at the bottom of caves also did not show luminescence (Figure 12k,l).

Cathode luminescence showed that cements in the upper part of karst caves in Well LG43-1 showed three phases of luminescence. The Phase 1 luminescence zone reflected a meteoric freshwater environment. Phase 2 was characterized by a weak luminescence zone and reflected a freshwater–seawater mixed environment. The Phase 3 luminescence zone reflected a meteoric freshwater environment. Therefore, it was inferred that this class of karst pore cement in the upper part of karst caves was formed in a rapidly changing karst environment, possibly near coastal margins. Additionally, fillings in the lower part of karst caves generally did not show luminescence (for either grains or calcite), and the electron microprobe analysis showed a low Mn content, indicating calcite precipitated in seawater.

## 6.2. Trace Elements Testing of Fillings and Identification of Paleokarst Environments

The chemical and trace element composition of calcite, clay, and limestone grains in karst cave fillings, as well as calcarenite grains and calcite cements among calcarenite grains in the upper part of karst caves, were mainly analyzed using an electron microprobe. The results are shown in Table 1. Sr/Ba and Fe/Mn ratios were used to identify paleokarst environments [33,35–38]. Previous research has indicated that the Sr/Ba ratio in clay or mudstone increases with salinity. Ratios >1 indicate marine sedimentation and those <1 indicate continental sedimentation [33,35–37]. However, Fe/Mn ratios of 1 indicate normal seawater salinity, while Fe/Mn < 1 indicates highly saline water, and ratios of 5 or greater indicate freshwater sedimentation. Therefore, the higher the Fe/Mn ratio, the lower the salinity [33,37,38].

**Table 1.** The components analyzed by electron microprobe and calculating the results of the main parameters of bedrocks and fillings in upper karst caves.

Spot ID	Analyzing Item	MgO (wt %)	Al <sub>2</sub> O <sub>3</sub> (wt %)	SiO <sub>2</sub> (wt %)	K <sub>2</sub> O (wt %)	CaO (wt %)	Mn (ppm)	Fe (ppm)	Fe/Mn	Sr (ppm)	Ba (ppm)	Sr/Ba	Identification of Paleokarst Environment		
													Sr/Ba	Fe/Mn	Environments
a-1	Calcite in karst caves	0.042	0.392	0.604	0.199	55.050	0	529	/	0	0	/	/	<1	Cannot identify
a-2		0.018	0.032	0.037	0.040	55.649	403	54	0.13	0	179	0			
a-3		0.019	0.042	0.136	0.059	55.746	279	443	1.59	0	0	/			
a-4	Limestone grains in karst caves	0.194	0.094	0.070	0.028	55.546	116	0	0	152	0	/	>1	/	Seawater
a-5		0.197	0.343	0.590	0.102	55.027	62	342	5.52	0	18	0	<1	≈5	Freshwater
a-6		0.404	0.038	0.132	0.063	55.269	0	490	/	381	0	/	>1	/	Seawater
a-7	Clay in karst caves	2.040	28.133	41.72	10.722	0.766	318	12,903	40.58	0	152	0	<1	>5	Freshwater
a-8		2.069	26.849	39.381	9.815	1.213	372	6510	17.50	0	152	0			
a-9		1.927	27.916	41.316	10.239	1.262	225	6844	30.42	0	242	0			
b-1	Calcite in karst caves	0.198	1.010	1.661	0.267	53.479	0	1680	/	0	0	/	>1	≈1	Seawater
b-2		0.076	0.153	0.203	0.058	55.497	0	529	/	0	0	/			
b-3		0.132	0.566	0.267	0.018	55.082	132	210	1.59	676	0	/			
c-1	Calcite in karst caves	0.070	0.081	0.187	0.046	55.593	0	319	/	617	125	4.94	>1	/	Seawater
c-2		0.018	0.039	0.180	0.014	55.785	0	506	/	0	0	/			
c-3		0.086	0.197	0.409	0.041	55.246	0	1291	/	0	0	/			
d-1	Calcite cement of calcarenite in upper karst caves	0.150	0.065	0.172	0.012	55.525	0	630	/	592	0	/	>1	≈1	Seawater
d-2		0.088	0.112	0.079	0.014	55.696	0	482	/	0	0	/			
d-3		0.132	0.566	0.267	0.018	55.082	132	210	1.59	676	0	/			
e-1	Arenite grains of calcarenite in upper karst caves	0.208	0.097	0.153	0	55.462	0	179	/	0	0	/	>1	≈5	Freshwater
e-2		0.168	0.574	0.385	0	55.034	85	389	4.58	101	215	0.47			
e-3		0.179	0.033	0.119	0.010	55.648	0	0	/	0	0	/			

Electron microprobe analysis of calcite and limestone grains in karst cave fillings were characterized by  $Sr/Ba > 1$  and  $Fe/Mn \approx 1$  (Figure 13a–c, Table 1). These ratios support the theory that limestone grains and calcite inside karst caves originated from a seawater environment since clay minerals in karst caves showed  $Sr/Ba < 1$  and  $Fe/Mn > 5$  (Figure 13a, Table 1) [35–38]. Additionally, the electron microprobe analysis of calcarenite in the upper part of karst caves showed  $Sr/Ba < 1$  and  $Fe/Mn \approx 5$  (Figure 13d, Table 1), indicating that karst cave formation and clay filling were affected by meteoric freshwater [35–38]. Therefore, it was interpreted that the formation of karst caves in Well LG43-1 was controlled by meteoric freshwater and mixed-water dissolution, where the clay fillings inside karst caves were of freshwater origin, and calcite was precipitated in seawater. Thus, the formation and filling of karst caves may have occurred in a coastal margin environment.

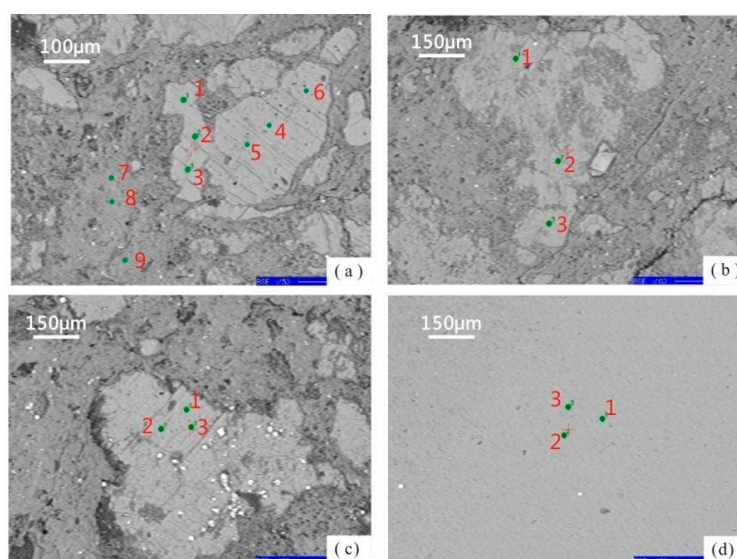


**Figure 13.** The electron microprobe analysis spots of fillings in Well LG43-1. (a) Spots 1–3 were located above the calcite in karst cave; spots 4–6 were located above limestone grains in karst cave; spots 7–9 were located above the clay in the karst cave; (b) Spots 1–3 were located above the calcite in the karst cave; (c) Spots 1–3 were located above the calcite in karst cave; (d) Spots 1–3 were located above the arenite grains of calcarenite in the upper karst cave.

## 7. Paleokarst Types and Genetic Model of the Yingshan Formation Karst in the Northern Slope of the Tazhong Area

### 7.1. Comparison between the Yingshan Formation Karst Characteristics and Modern Karst Types

Based on our results, the karsts of the Yingshan Formation in the northern slope of the Tazhong area have the following characteristics: (1) Exposure occurred soon after sedimentation, leading to karstification, with an exposure time of 7–11 Ma. (2) Solution pores and caves with no structural texture show Swiss cheese-like dissolution features and spongy dissolution zones. The pores are primarily filled with gravels, clay, and calcite, and a pit cenote at the top of the Yingshan Formation in Well LG111. (3) Most karst pores and caves are developed within 50 m below the unconformity, and single karst caves are generally between 0.1–3.0 m high, but their widths can range up to one hundred meters. Seismic attribute analysis indicates that these pores and caves are distributed over a large area, and it is comprehensively inferred that karst pore-cave systems comprise a network of crosscutting pipe-like caves. (4) Cathode luminescence and electron microprobe analyses indicate that clay fillings in karst caves are of freshwater origin, and calcite is of seawater origin. Pore cements show three phases of cathode luminescence, indicating an alternating freshwater and seawater environment. (5) The reservoirs commonly develop in the lower part of filled intervals. The features described above

differ from long-term exposed buried hill (or typical continental) karsts, and cannot be explained as continental freshwater karsts. However, they can be explained as eogenetic karsts.

Modern studies of eogenetic karsts suggest that carbonate does not form under eogenetic conditions. Rather, soft rock karsts with high porosity and permeability form instead [39]. Even so, large solution cavities may be developed under such conditions [40–42]. For example, large-sized flank-margin caves have been found on the periphery of modern carbonate islands [43–45]. Additionally, Smart et al. [46] reported that eogenetic karstification resulted from large-area exposure soon after the formation of a large-scale carbonate platform in the Yucatan Peninsula of Mexico, where cross-linked anastomosing cave systems were also found. The study found that the mixed-water dissolution in the seawater–freshwater mixing zone resulted in the formation of eogenetic karst caves [39]. The Yucatan Peninsula study of Lace and Mylroie [39] provided a reference model for studying karst cave genesis formed during short-term exposure. Some scholars have used this pore development model of karst formation for reference when studying the formation of paleokarst pores-caves using outcrop investigation, core, seismic attribute, and other methods [16,47,48]. Karsts in the Tazhong area display different characteristics from karsts in modern island settings. Karst caves in islands are dominated by flank-marginal caves and develop near coastal margins, but either decrease in abundance or do not develop toward island centers [43–45]. These patterns are not reflected in the large areal distribution of pores and caves in the Tazhong area. Additionally, modern island karsts have small catchment areas, differing greatly from the exposed karsts in medium–large-sized carbonate platforms, and are more similar to the exposed platform karsts found in the Yucatan Peninsula in Mexico [39].

Comparison with the exposed platform karsts of the Yucatan Peninsula in Mexico shows high similarities in exposure time (several Ma), exposure type (carbonate platform), karst shape (both have spongy dissolution zones), fracture pore-cave development characteristics (both have a network of crosscutting, pipe-like cave systems), and filling characteristics (pore-caves are largely filled). Additionally, geochemical characteristics indicate the paleokarsts formed in an alternating seawater–freshwater environment, which further suggests the karsts of the Yingshan Formation are extremely similar to the eogenetic karsts of the Yucatan Peninsula in Mexico. The latter can be taken as a reference for the study of pore and cave development in the northern slope of the Tazhong area.

### *7.2. Development Model of Pores and Caves Controlled by Eogenetic Karsts*

Eogenetic karst pores and caves of the Yucatan Peninsula in Mexico were mainly developed in freshwater–seawater mixed dissolution zones, and were primarily controlled by changes in sea level [39,46]. Statistical comparison of filled intervals and non-filled intervals of the Yingshan Formation showed that the formation of pores and caves was controlled by three phases of mixed-water dissolution, representing three periods of relatively stable sea level (Figure 14). The Sandbian-Katian sea Level curve was obtained by continuous sampling of sediments from the Tumuxiuke Formation and Lianglitage Formation on a regional scale. This curve indicated three changes in sea level [49]. From the study of Well Sn5 in the eastern part of the No. 1 fault belt of the Tazhong Area, it was found that nearly 20 m of the Tumuxiuke Formation was developed above the Yingshan Formation (Figure 15) [27]. In the present study area, intervening strata between the Tumuxiuke Formation and the Liang-3 depositional stage continuously overlie the Yingshan Formation, suggesting that the Yingshan Formation underwent the transgression after exposure. The Liang-5 and Liang-4 depositional stages and the Tumuxiuke Formation represent three periods of relatively stable sea level, which correspond to three sections that developed pores and caves (Figure 15).

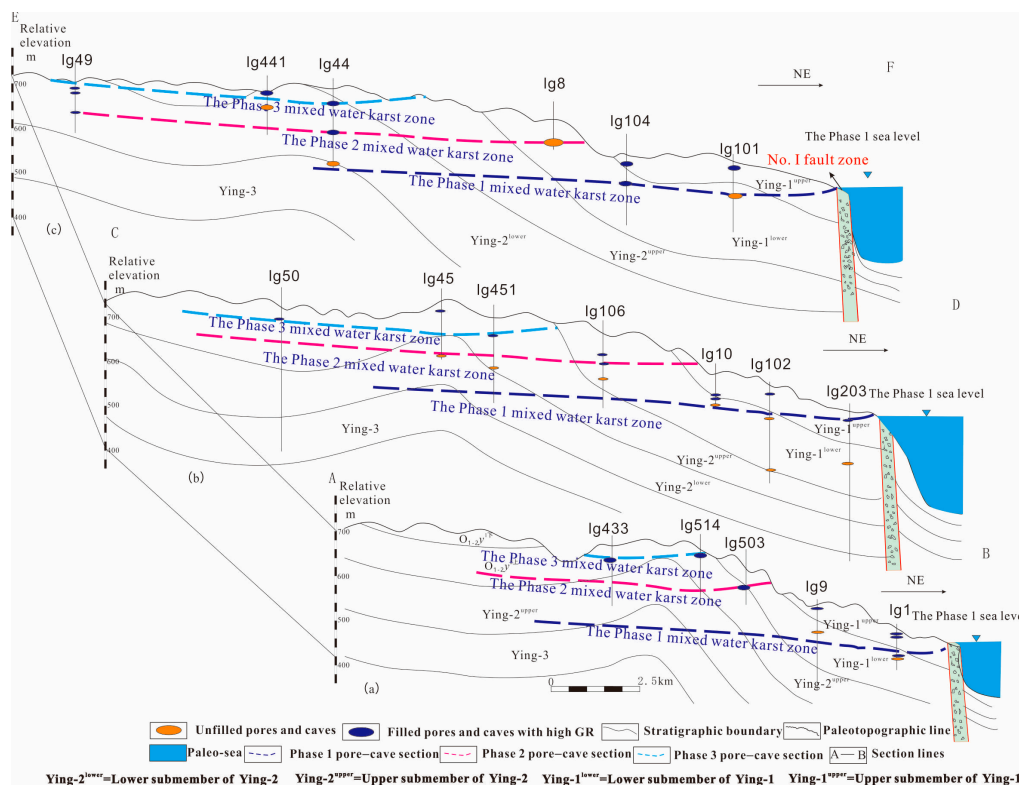


**Figure 14.** Three sections that developed pores and caves represent three phases of relatively stable sea level in the northern slope, Tazhong area. (a–c) respectively represent three sections that developed pores and caves from different locations. The development of the phase 3 pore-cave section showed a good correlation across the different locations. Each phase of the pore-caves in plain view exhibits cross-linked anastomosing network characteristics. The network distribution was developed by eogenetic karstification of the mixing-water under the control of sea level during that phase. The three sections of pore-caves in the Yingshan Formation were controlled by three phases of sea level. Paleotopographic lines were drawn based on the paleogeomorphic restoring technique of Deng et al. [50]. The plane locations of section lines are shown in Figure 11.

Previous research has indicated that there is no absolute stable sea level, so the relatively stable sea level refers to periods of weak sea level fluctuation, varying within ten meters or less, where the sea level rise and fall is controlled by global interglacial periods [39,46]. During interglacial periods, high sea levels (the highstand period) led to the formation of a network of crosscutting, pipe-like pores or caves in mixed dissolution zones. When the sea level dropped (lowstand period), pipe-like caves in the early mixed zones were exposed. Some caves collapsed because rocks were weakly consolidated and prone to collapse. When the surface collapsed, pit cenotes were formed. Surface freshwater dissolution produced clay that entered the karst caves and, along with seepage water, was deposited to form argillaceous fillings. When the sea level rose again (interglacial period), clay in seawater together with gravel derived from surface freshwater dissolution filled the fractures and caves. If the pores and caves were located in seawater undercurrent zones, calcite precipitated and quickly filled the karst caves.

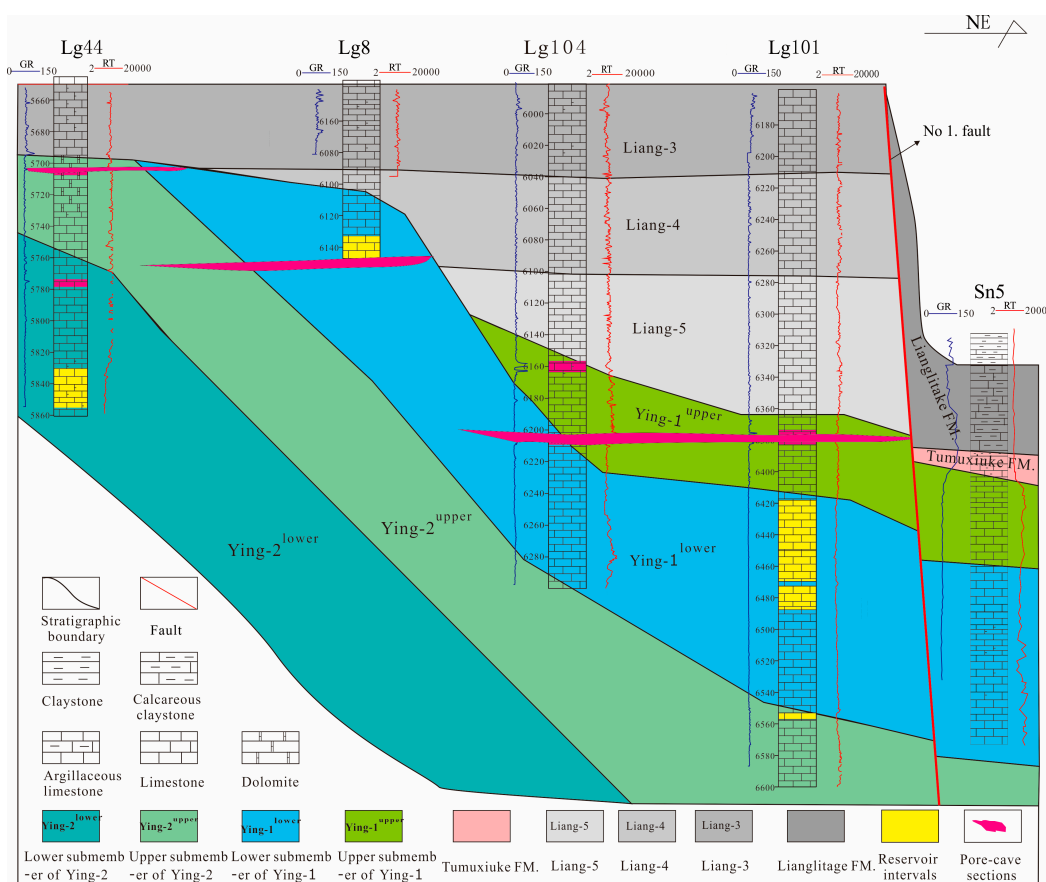


**Figure 15.** The comparison diagram of the Yingshan Formation and Lianglitage Formation in the Northern Slope, Tazhong Area (Liang-3 Top Level). An unconformable contact is interpreted between the Yingshan Formation and Lianglitage Formation. In the interval from the Tumuxiuke Formation to the Liang-3 depositional stage, the strata constantly overlie the Yingshan Formation, suggesting that the Yingshan Formation underwent the transgression after exposure. The Tumuxiuke Formation, Liang-5, and Liang-4 depositional represent three periods of relatively stable sea level, which correspond to three sections that developed pores and caves. In addition, Well Sn5 is located east of the No. 1 fault in the Tazhong Area where sediments of the Lianglitage Period were interpreted as a deep-water facies comprising marlstone and lime mudstone. The lithology and thickness of these facies are obviously different from the platform facies intersected in the four wells west of the No. 1 fault (the distribution of wells is shown in Figure 11).

The sequence of events as formulated above represents a new model for the development and filling of pores and caves affected by sea level fluctuation. The northern slope of the Tazhong area underwent three phases of relatively stable sea level where the development and filling of pores and caves were controlled by sea level change (Figure 16). Previous pore-cave systems were filled during the transgressive stage of the Lianglitage Period. Further, the pressure of newly deposited sediment led to the collapse and compaction of existing pore space, leaving only smaller pore spaces in the lower part of the Yingshan Formation. This resulted in the formation of the present-day reservoirs.

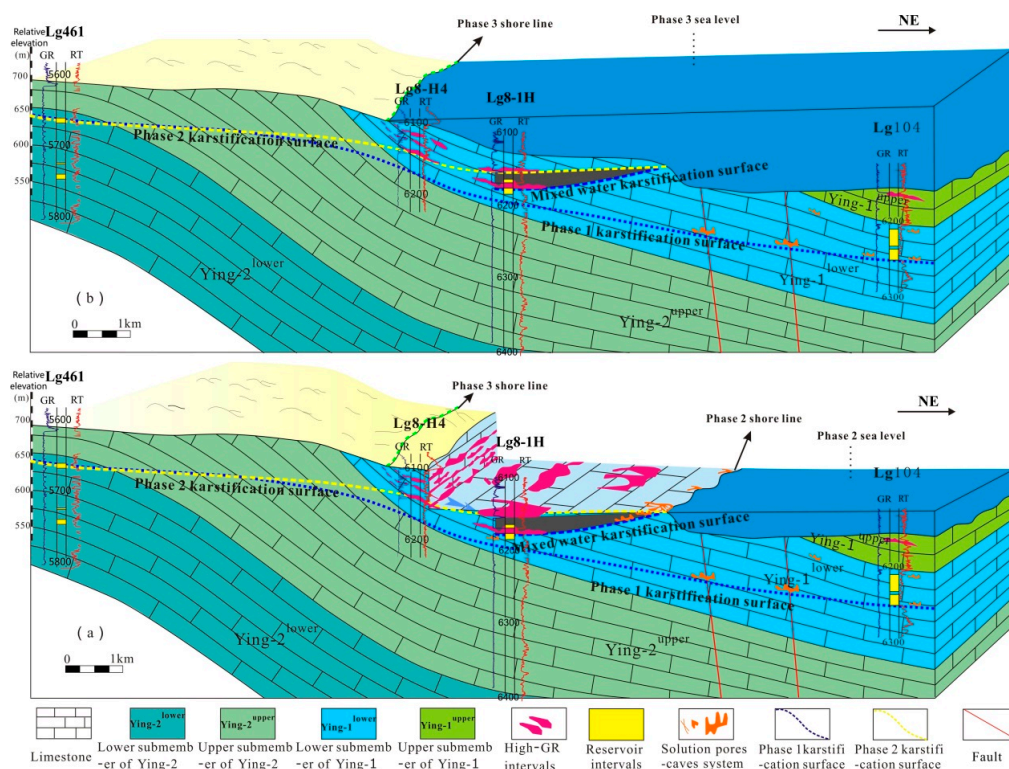


**Figure 16.** The filling and development model for karst caves in the Yingshan Formation in the northern slope of the Tazhong area. (a) The development of the karst pore-caves was dominated by the karstification of the eogenetic mixing-water under the control of phase 2 sea level. Pore-caves formed a cross-linked anastomosing network in plain view; (b) when sea level rose, the development of the karst pore-caves was dominated by the karstification of the eogenetic mixing-water under the control of the phase 3 sea level. However, phase 2 pore-caves were filled with mud and calcite cements. Furthermore, as the overburden pressure increased, most of the pore-caves collapsed and spaces within pore-caves of phase 2 decreased.

## 8. Conclusions

The results from this study on the genesis of paleokarst pore-caves in the Yingshan Formation represent a major contribution towards the formulation of paleokarst models. The carbonate platform of the Yingshan Formation was uplifted after the first episode of middle Caledonian tectonic activity when it was exposed for about 7–11 Ma. The formation then underwent intense karstification, resulting in the formation of alveolar-like karst pores, Swiss cheese-like karst pores, spongy-like dissolution zones, pit cenotes, and horizontally continuous small karst caves. Based on the statistical analysis, it was found that most karst pore-caves are located within 50 m below the unconformity. The caves generally range in height from 0.1–3.0 m but reach up to hundreds of meters in width. Moreover, pore-caves are frequently filled with mixtures of gravel, clay, and calcite. Horizontal well and seismic attribute analyses showed that these pore-caves are widely distributed on a horizontal plane, and hence it is concluded that the interpreted cross-linked anastomosing network of horizontal cave passages is coincident with the plane of the Yingshan Formation karst pore-cave system in the Tazhong area. These features further suggest the Yingshan Formation contains eogenetic karsts that are similar to the eogenetic karsts of the Yucatan Peninsula in Mexico. Further, the Yingshan Formation pore-caves mainly developed in the mixed freshwater–seawater saturated karst zone, and were affected by sea level. Meanwhile, geochemical data from karst cave fillings in the Yingshan Formation indicate that the fillings were deposited in a mixed seawater–freshwater environment. Compared to pore-caves, it was found that three sections of mixed-saturated karst developed in the Yingshan Formation during

the period of exposure. As a result, the development of karst pore-caves in the Yingshan Formation of the northern Tazhong slope was dominated by eogenetic mixed-water karstification under the control of three phases of relatively stable sea levels.

**Author Contributions:** Conceptualization, Y.D.; Methodology, Y.Y.; Formal Analysis, Y.D.; Investigation, J.L. and Q.Z.; Writing-Original Draft Preparation, Y.D.; Writing-Review & Editing, L.L.; Project Administration, B.L. and J.C.; All the co-authors performed a critical revision of the intellectual content of the paper.

**Funding:** This research was funded by the Nonprofit Industry Research Program of the Chinese Academy of Geological Sciences (YYWF201723), the Geological Survey Program of the China Geological Survey (DD20179012, DD20190562), the Natural Science Foundation of Guangxi, China (2016GXNSFAA380185), and the National Science and Technology Major Project of the Ministry of Science and Technology of China (2017ZX05008005-010).

**Acknowledgments:** Pan Wen-Qing and Senior Engineer Zhang Zheng-Hong of the Research Institute of Exploration and Development at Tarim Oilfield Company of PetroChina were of great assistance during core observation and sample collection. Zhong Yi-Jiang of Chengdu University of Technology has been of great support during samples testing and analysis processes.

**Conflicts of Interest:** The authors declare no conflict of interest.

## References

1. Yuan, D.X. *China Karstology*; Geology Press: Beijing, China, 1993; pp. 4–8. (In Chinese)
2. James, N.P.; Choquette, P.W. *Paleokarst*; Springer: New York, NY, USA, 1988; pp. 6–10.
3. Meyers, W.J. Paleokarstic Features on Mississippian Limestone, New Mexico. In *Paleokarst*; James, N.P., Choquette, P.W., Eds.; Springer: New York, NY, USA, 1988; pp. 306–328.
4. Kerans, C. Karst-controlled reservoir heterogeneity in Ellenburger Group carbonates of west Texas. *AAPG Bull.* **1988**, *72*, 1160–1183.
5. Lucia, F.J. Lower Paleozoic cavern development, collapse, and dolomitization, Franklin Mountains, El Paso, Texas. In *Unconformities and Porosity in Carbonate Strata*; Budd, D.A., Saller, A.H., Harris, P.M., Eds.; AAPG Memoir 63: Tulsa, OK, USA, 1995; pp. 279–300.
6. Loucks, R.G. Paleocave carbonate reservoirs: Origins, burial depth modifications, spatial complexity and reservoir implications. *AAPG Bull.* **1999**, *83*, 1795–1834.
7. Li, J.; Zhang, W.; Luo, X.; Hu, G. Paleokarst reservoirs and gas accumulation in the Jingbian field, Ordos Basin. *Mar. Pet. Geol.* **2008**, *25*, 401–415. [[CrossRef](#)]
8. Dan, Y.; Liang, B.; Cao, J.W.; Zhang, Q.Y.; Hao, Y.Z. Characteristics and genesis of Ordovician carbonate karst reservoir in the shallow coverage zone of Halahatang area, northern Tarim Basin. *Geophys. Prospect. Pet.* **2015**, *54*, 90–98. (In Chinese)
9. Zhao, W.Z.; Shen, A.J.; Pan, W.Q.; Zhang, B.M.; Qiao, Z.F.; Zheng, J.F. A research on carbonate karst reservoirs classification and its implication on hydrocarbon exploration: Cases studies from Tarim Basin. *Acta Petrol. Sin.* **2013**, *29*, 3213–3222. (In Chinese)
10. Zhao, W.Z.; Shen, A.J.; Hu, Y. Geological conditions and distributional features of large-scale carbonate reservoirs onshore China. *Pet. Explor. Dev.* **2012**, *39*, 1–12. (In Chinese) [[CrossRef](#)]
11. Kang, Y.Z. Palaeokarst of Cambro-Ordovician and oil-gas distribution in Tarim Basin. *Xinjiang Pet. Geol.* **2005**, *26*, 472–480. (In Chinese)
12. Zhu, G.Y.; Zhang, S.C.; Wang, H.H.; Yang, H.J.; Meng, S.C.; Gu, Q.Y. The formation and distribution of deep weathering crust in north Tarim Basin. *Acta Petrol. Sin.* **2009**, *25*, 2384–2398. (In Chinese)
13. Zeng, H.L.; Loucks, R.; Janson, X.; Wang, G.Z.; Xia, Y.P.; Yuan, B.H.; Xu, L.G. Three-dimensional seismic geomorphology and analysis of the Ordovician paleokarst drainage system in the central Tabei Uplift, northern Tarim Basin, western China. *AAPG Bull.* **2011**, *95*, 2061–2083. [[CrossRef](#)]
14. Gu, J.Y. Characteristics and evolutionary model of karst reservoir of Lower Ordovician carbonate rocks in Lunnan area of Tarim Basin. *J. Palaeogeogr.* **1999**, *1*, 54–60. (In Chinese)
15. Jin, Z.J.; Zhu, D.Y.; Hu, W.X.; Zhang, X.F.; Zhang, J.T.; Song, Y.C. Mesogenetic dissolution of the middle Ordovician limestone in the Tahe oilfield of Tarim Basin, NW China. *Mar. Pet. Geol.* **2009**, *26*, 753–763. [[CrossRef](#)]

16. Xiao, D.; Tan, X.C.; Xi, A.H.; Liu, H.; Shan, S.J.; Xia, J.W.; Cheng, Y.; Lian, C.B. An inland facies-controlled eogenetic karst of the carbonate reservoir in the Middle Permian Maokou Formation, southern Sichuan Basin, SW China. *Mar. Pet. Geol.* **2016**, *72*, 218–233. [[CrossRef](#)]
17. Dan, Y.; Liang, B.; Cao, J.W.; Zhang, Q.Y.; Hao, Y.Z. Eogenetic karstification in carbonate and its significance for hydrocarbon geology. *Carsologica Sin.* **2015**, *34*, 126–134. (In Chinese)
18. Vacher, H.L.; Mylroie, J.E. Eogenetic karst from the perspective of an equivalent porous medium. *Carbonates Evaporites* **2002**, *17*, 182–196. [[CrossRef](#)]
19. Yang, H.J.; Han, J.F.; Sun, C.H. A development model and petroleum exploration of karst reservoirs of Ordovician Yingshan formation in the northern slope of Tazhong palaeouplift. *Acta Petrolei Sin.* **2011**, *32*, 199–205. (In Chinese)
20. Feng, R.W.; Ou, Y.C.; Pang, Y.J.; Li, Z.Z.; Luo, X.; Zhang, Q.; Li, S.Y.; Zhou, Y.; Cheng, L. Evolution modes of interbedded weathering crust karst: A case study of the 1st and 2nd members of Ordovician Yingshan Formation in EPCC block, Tazhong, Tarim Basin. *Pet. Explor. Dev.* **2014**, *41*, 49–59. [[CrossRef](#)]
21. Ni, X.F.; Shen, A.J.; Pan, W.Q. Geological modeling of excellent fractured-vuggy carbonate reservoirs: A case study of the Ordovician in the northern slope of Tazhong palaeouplift and the southern area of Tabei slope, Tarim Basin. *Pet. Explor. Dev.* **2013**, *40*, 414–422. [[CrossRef](#)]
22. Lan, X.D.; Lü, X.X.; Zhu, Y.M. Characteristics and differential accumulation of oil/gas in Lower Paleozoic marine carbonate on northern slope of Tazhong Low Rise, Tarim Basin, NW China: A case study of Lower Ordovician Yingshan Formation. *Arab. J. Geosci.* **2014**, *7*, 4487–4498. [[CrossRef](#)]
23. Yu, J.B.; Li, Z.; Yang, L. Characterization and distribution of deeply-buried paleokarst carbonate reservoirs of Ordovician Yingshan Formation in northern slope of central Tarim Basin. *Acta Petrolei Sin.* **2016**, *37*, 299–310. (In Chinese)
24. Yu, J.B.; Li, Z.; Yang, L. Fault system impact on paleokarst distribution in the Ordovician Yingshan Formation in the central Tarim Basin, northwest China. *Mar. Pet. Geol.* **2016**, *71*, 105–118. [[CrossRef](#)]
25. Yu, H.F.; Bai, Z.K.; Deng, L.P. Determination and geologic significance of Yingshan unconformity of lower Ordovician in Tazhong area, Tarim Basin. *Xinjiang Pet. Geol.* **2011**, *32*, 231–234. (In Chinese)
26. Zhang, H.; Cai, Z.X.; Qi, L.X.; Yun, L. Types and characteristics of eogenetic karst in the Yingshan Formation in northwestern Tazhong area, Tarim Basin. *Oil Gas Geol.* **2016**, *37*, 291–303. (In Chinese)
27. Chen, H.H.; Wu, Y.; Zhu, H.T. Eogenetic karstification and reservoir formation model of the Middle-Lower Ordovician in the northeast slope of Tazhong Uplift, Tarim Basin. *Acta Petrolei Sin.* **2016**, *37*, 1231–1246. (In Chinese)
28. Kang, Y.; Kang, Z. Tectonic evolution and oil and gas of Tarim Basin. *J. Southeast Asian Earth Sci.* **1996**, *13*, 317–325.
29. Lü, X.X.; Jin, Z.J.; Liu, L.F. Oil and gas accumulations in the Ordovician carbonates in the Tazhong Uplift of Tarim Basin, west China. *J. Pet. Sci. Eng.* **2004**, *41*, 109–121. [[CrossRef](#)]
30. Qu, H.Z.; Wang, Z.Y.; Yang, H.J. Karstification of reef-bank facies carbonate and its control on pore distribution: A case study of Upper Ordovician Lianglitage Formation in eastern Tazhong area, Tarim Basin, NW China. *Pet. Explor. Dev.* **2013**, *40*, 592–598. [[CrossRef](#)]
31. Pang, H.; Chen, J.Q.; Pang, X.Q. Key factors controlling hydrocarbon accumulations in Ordovician carbonate reservoirs in the Tazhong area, Tarim basin, western China. *Mar. Pet. Geol.* **2013**, *43*, 88–101. [[CrossRef](#)]
32. Huang, S.J. The cathodeluminescence and diagenesis of the carbonates of Guanwushan Formation, middle Devonian, Ganxi, northwestern Sichuan. *J. Chengdu College Geol.* **1988**, *15*, 50–56. (In Chinese)
33. Huang, S.J. *Carbonate Diagenesis*; Geology Press: Beijing, China, 2010; pp. 100–101. (In Chinese)
34. Mussman, W.J.; Read, J.F. Sedimentology and development of a passive to convergent margin unconformity—Middle Ordovician Knox unconformity, Virginia Appalachians. *Geol. Soc. Am. Bull.* **1986**, *97*, 282–324. [[CrossRef](#)]
35. Katchenkov, S.M. Element distributions in clay minerals. *Dokl. AN SSSR* **1960**, *134*, 680–683. (In Russian)
36. Katchenkov, S.M.; Flegontova, Y.I. Minor elements in Indian-Ocean muds. *Trans. All-Union Pet. Geol. Res. Inst.* **1964**, *227*, 202–211. (In Russian)
37. Deng, H.W.; Qian, K. *Sedimentary Geochemistry and Environmental Analysis*; Science Technique Press: Gansu, China, 1993; pp. 78–94. (In Chinese)
38. Lizinikov, A.H. *Phase and Construction of Deposit Rock*; Science Press: Beijing, China, 1961; pp. 150–155. (In Chinese)

39. Lace, M.J.; Mylroie, J.E. *Coastal Karst Landforms*; Springer: Dordrecht, The Netherlands; Heidelberg, Germany; New York, NY, USA; London, UK, 2013; pp. 1–300.
40. Mylroie, J.E.; Jenson, J.W.; Taborosi, D. Karst features of Guam in terms of a general model of carbonate island karst. *J. Cave Karst Stud.* **2001**, *63*, 9–22.
41. Moore, P.J.; Martin, J.B.; Sreaton, E.J.; Neuhoff, P.S. Conduit enlargement in an eogenetic karst aquifer. *J. Hydrol.* **2010**, *393*, 143–155. [[CrossRef](#)]
42. White, S.; Webb, J.A. The influence of tectonics on flank margin cave formation on a passive continental margin: Naracoorte, Southeastern Australia. *Geomorphology* **2015**, *229*, 58–72. [[CrossRef](#)]
43. Mylroie, J.E.; Carew, J.L.; Vacher, H.L. Karst development in the Bahamas and Bermuda. In *Terrestrial and Shallow Marine Geology of the Bahamas and Bermuda*; Curran, H.A., White, B., Eds.; Geological Society of America Special Paper: Colorado Boulder, CO, USA, 1995; pp. 251–267.
44. Mylroie, J.E.; Carew, J.L. Speleogenesis in coastal and oceanic settings. In *Evolution of Karst Aquifers*; Klimchouk, A.B., Ford, D.C., Palmer, A.N., Eds.; National Speleological Society: Huntsville, Alabama, USA, 2000; pp. 26–33.
45. Mylroie, J.E.; Carew, J.L. Karst development on carbonate islands. *Speleogenesis Evol. Karst Aquifers* **2003**, *1*, 1–21.
46. Smart, P.L.; Beddows, P.A.; Coke, J.; Doerr, S.; Smith, S.; Whitaker, F.F. Cave development on the Caribbean coast of the Yucatan Peninsula, Quintana Roo, Mexico. In *Perspectives on Karst Geomorphology, Hydrology, and Geochemistry*; Harmon, R.S., Wicks, C., Eds.; Geological Society of America Special Paper 404: Boulder, CO, USA, 2006; pp. 105–128.
47. Baceta, J.I.; Wright, V.P.; Beavington-Penney, S.J.; Pujalte, V. Palaeohydrogeological control of palaeokarst macro-porosity genesis during a major sea-level lowstand: Danian of the Urbasae Andia Plateau, Navarra, North Spain. *Sediment. Geol.* **2007**, *199*, 141–169. [[CrossRef](#)]
48. Dou, Q.F.; Sun, Y.F.; Sullivan, C. Paleokarst system development in the San Andres Formation, Permian Basin, revealed by seismic characterization. *J. Appl. Geophys.* **2011**, *75*, 379–389. [[CrossRef](#)]
49. Hu, M.Y.; Qian, Y.; Hu, Z.G.; Wang, Y.Q.; Xiang, J. Carbon isotopic and element geochemical responses of carbonate rocks and Ordovician sequence stratigraphy in Keping area, Tarim Basin. *Acta Petrol. Mineral.* **2010**, *29*, 199–205. (In Chinese)
50. Deng, X.L.; Zhang, Q.Y.; Liang, B.; Dan, Y. Reconstruction of karst palaeogeomorphology for the Ordovician Yingshan Formation in the central Tarim Basin. *Carsol. Sin.* **2015**, *34*, 154–158. (In Chinese)



© 2018 by the authors. Licensee MDPI, Basel, Switzerland. This article is an open access article distributed under the terms and conditions of the Creative Commons Attribution (CC BY) license (<http://creativecommons.org/licenses/by/4.0/>).